ELSEVIER

Journal of Structural Geology 28 (2006) 36–49

JOURNAL OF STRUCTURAL GEOLOGY

www.elsevier.com/locate/jsg

Thrust dip and thrust refraction in fault-bend folds: analogue models and theoretical predictions

Bertrand Maillot [a,*], Hemin Koyi [b]

[a] *Dépt. des sciences de la Terre et de l'environnement, Université de Cergy-Pontoise, CNRS UMR 7072, 5, mail Gay Lussac, Neuville-sur-Oise, 95031 Cergy-Pontoise cedex, France*

[b] *Department of Earth Sciences, Hans Ramberg Tectonic Laboratory, Uppsala University, Villav. 16, 752 36 Uppsala, Sweden*

Received 14 February 2005; received in revised form 28 September 2005; accepted 1 October 2005
Available online 1 December 2005

Abstract

Analogue models made of two layers of loose sand separated by a thin layer of micro glass beads were shortened by a rigid emerging ramp dipping at either 30° or 45° and possessing a high, intermediate, or null surface friction. Shortening resulted in formation of closely spaced back thrusts in the sand layers. The dips of the back thrusts vary within a range of 30° depending on the ramp friction, and 7° depending on its dip. An increase in ramp friction, or, to a lesser extent, in ramp dip, decreases the thrust dips in the model. The second important observation is that, when friction is greater along the ramp than along the layer of glass beads, then the glass beads layer acts as a separate upper ramp above which the back thrusts steepen. The theory proposed to explain these observations predicts the thrust dips through a two-step procedure: first, global equilibrium of forces in the two layers is required to yield the mean forces at stake along the ramps and thrusts, second, the total dissipation is minimized with respect to the dips of the back thrusts. The relevant frictional properties of our analogue materials have been measured in stress conditions as close as possible to the experimental ones (below 1 kPa), and used with the theory to yield optimal back thrust dips that are all within 3° of the measured dips. This is a surprisingly good fit when considering that we did not take into account geometric changes, strain-softening, and dilatancy or compaction, due to slip on the thrusts. We conclude that this general two-step theoretical procedure is validated in the context of analogue frictional materials. We also propose a possible mechanism for thrust refraction and top-to-the-foreland sense of shear observed in the hanging walls of lower-flat to ramp transition in sedimentary piles that is based on the triggering of secondary upper ramps. Finally, this mechanical approach can also be seen as complementary to the kinematic models of fold-thrust structures which, by definition, cannot grasp the strong effects of friction on the kinematics.

Keywords: Fault-bend fold; Analogue modelling; Minimum dissipation; Thrust refraction; Mechanics

1. Introduction

The transport of a sedimentary sequence from a thrust flat ('décollement') to a thrust ramp (Rich, 1934) is a regular occurring process in fold-thrust belts. The evolution of flat-ramp structures have been established with the help of kinematic models such as the fault-bend fold (Suppe, 1983, and numerous articles, e.g. Zoetemeijer and Sassi, 1992). A very important characteristic of these processes is the localisation of deformation into narrow ductile hinges ('kinks'), or into frictional thrusts (e.g. Laubscher, 1976; Boyer, 1986), which are precisely rooted at flat-ramp transition, i.e. at the fault bends. In most of the kinematic models these kink surfaces are assumed to bissect the angle between the flat and the ramp in order to conserve the thickness of the sedimentary layers. Although this is a widely used approximation for the balancing of cross-sections at a belt scale, it is clearly insufficient for the study of single structures. Some early kinematic models assumed a vertical kink plane (e.g. Endignoux and Mugnier, 1990), which led to a thinning of the ramp hanging wall as observed at a crustal scale in the Southern Alps by Little et al. (2002). Two recent models describe a thickening of the sedimentary layers (Cristallini and Allmendinger, 2002; Buil, 2002).

* Corresponding author. Tel.: +33 1 34 25 73 59; fax: +33 1 34 25 73 50.
E-mail address: bertrand.maillot@u-cergy.fr (B. Maillot).

0191-8141/$ - see front matter © 2005 Elsevier Ltd. All rights reserved.
doi:10.1016/j.jsg.2005.10.001

Maillot and Leroy (2003) have proposed to enrich this kinematic approach with the mechanical concepts of global force balance and minimum dissipation. They adopted the concepts from Merchant (1944, 1945), who proposed it in the context of metal-cutting. In fact, the present paper follows Merchant's experimental approach to validate his theory. In their theoretical paper, Maillot and Leroy (2003) predicted that for frictional homogeneous materials, the dips of the thrusts are as much, or more, controlled by the frictional properties than by the ramp dip. Luu (2003) has also generalised the theory to a multi-layer frictional hanging wall with the help of limit analysis, and Luu et al. (2004) have done a parametric study of a three layer hanging wall, which suggests a possible mechanism for thrust refraction across beds, and for top-to-the-foreland shear. Although the back thrust dips predicted by Maillot and Leroy (2003) were shown to be in good agreement with the dips observed in analogue (Merle and Abidi, 1995; Bonini et al., 2000) and numerical experiments (Erickson et al., 2001), a dedicated experimental verification of this theory was clearly required. This is the first objective of this article. The second objective is to verify the mechanism for thrust refraction as deduced from the parametric study of Luu et al. (2004).

The contents of this article are as follows. We first develop the theory in a self-consistent manner applied to our experimental set up. This leads us to include the effect of cohesion that was disregarded in the analysis of Maillot and Leroy (2003). An example will allow the reader to understand how the optimal thrust dips result from the competing effects of the various sources of dissipation. We then present in Section 3 a series of six experiments whereby a model made of two layers of loose sand separated by a thin layer of micro glass beads is forced to thrust above a rigid ramp (Fig. 1). The experiments are all identical, except for the ramp dip (30 or 45°) and the ramp friction (see Table 1). The apparatus and the procedures used to measure the frictional properties of our materials are discussed in detail in this section. Finally, in Section 4, we analyze the results of experiments, validate the theoretical predictions, propose a theoretical generalization of the observations regarding the conditions for thrust refraction, and briefly describe a field example.

Table 1
List of experiments

Exp. no.	Lower ramp properties			
	Dip (φ) (°)	Friction angle (α_{R1}) (°)	Friction coefficient	Cohesion (c_{R1}) (Pa)
2	30	34.5–34.8	0.691 ± 0.004	-20 ± 6
3	30	22.8–23.3	0.426 ± 0.005	51 ± 11
4	30	0	0	0
8	45	34.5–34.8	0.691 ± 0.004	-20 ± 6
7	45	22.8–23.3	0.426 ± 0.005	51 ± 11
9	45	0	0	0

The models are identical in all six experiments. Only the dip and the friction of the lower rigid ramp is varied.

2. The theory

We present here the theory for a two layer model as illustrated in Fig. 2a. A rigid ramp (EA) is moving horizontally at an input velocity v_i towards an analogue model (AFHE) made of two layers of loose sand separated by a thin layer (GDB) of micro glass beads. Shortening results in the movement of the two layers (ABDE) and (BCD) at respective output velocities v_{o1} and v_{o2} parallel to the ramp (EA). We assume that there is no internal deformation and that the movement therefore occurs only along the thrust planes (EA) and (DB), which we will call 'ramp' 1 (or lower) and 2 (or upper), and along (ED) and (DC), which we will call 'back thrusts' 1 (or lower) and 2 (or upper), respectively. Our goal is to determine the dips θ_1 and θ_2 of these two back thrusts that minimize the dissipation of energy brought to the model by the movement of the ramp. The strategy is first to consider a given geometry and kinematics (Fig. 2a), second, to determine all mean forces acting in the model by requiring global

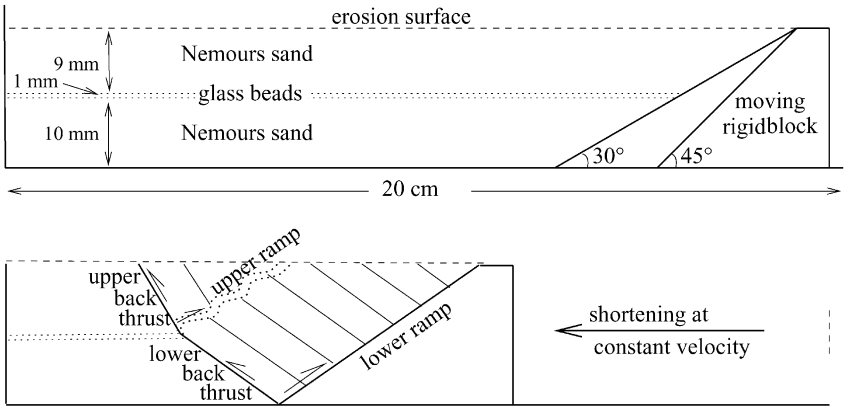

Fig. 1. Illustration of the experiments. Top: initial geometry of box and sample materials. In the six experiments presented here, the lower ramp dip may be 30 or 45°, and its surface has a null, intermediate, or high friction (see Table 1), everything else being identical. Bottom: typical steady state geometry of the back thrusts, and illustration of the terminology used in this article.

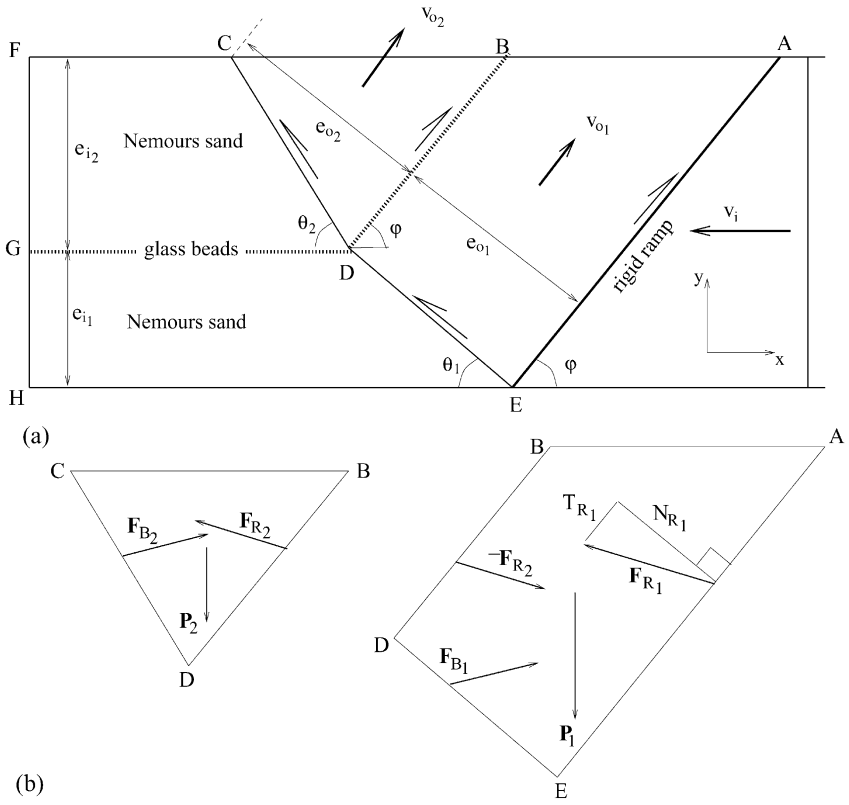

Fig. 2. (a) Illustration of the kinematic parameters. v_i, imposed velocity of rigid ramp (EA); v_{o1}, v_{o2}, velocities of lower (BDEA) and upper (BCD) sand layers relative to the rigid ramp. $e_{il,2}$, $e_{o1,2}$ thicknesses of sand layers as drawn. The semi-arrows indicate the sense of shear along the four thrust planes: ramps 1 and 2 (EA and DB) of dip φ; back thrusts 1 and 2 (ED and DC) of respective dips θ_1 and θ_2. (b) Free-body diagrams illustrating all forces considered: weights $\mathbf{P}_1$, and $\mathbf{P}_2$ of sections (BDEA, right) and (BCD, left); and forces $\mathbf{F}_{R1}$, $\mathbf{F}_{R2}$, $\mathbf{F}_{B1}$, $\mathbf{F}_{B2}$, acting, respectively, on ramps 1 and 2, and back thrusts 1 and 2. Note that these are total forces acting on each thrust plane, not forces acting on specific points. Decomposition into normal N_{R1} and tangential T_{R1} components is illustrated for $\mathbf{F}_{R1}$ only.

equilibrium (Fig. 2b), third, to calculate dissipations—from kinematics and forces—along all thrust planes and, fourth, to minimize the total dissipation with respect to the dips θ_1 and θ_2. We now develop these four stages in details.

2.1. Kinematics

We assume that the shortening process is in a steady state: the dips θ_1 and θ_2, and all other geometric parameters, are constant in time, and do not change with the amount of shortening. Any relief build-up is fully eroded along the surface line (AF) (Fig. 2). We assume that the back thrusts form continuously along the line (EDC) and that all the deformation is isochoric, and thus neglect dilatation or compaction due to slip along the thrust planes. Important kinematic relationships follow. First, velocity compatibility requires that the components of the velocities perpendicular to the back thrusts be equal on both sides of these planes:

$$\begin{aligned} v_i \sin\theta_1 &= v_{o1} \sin(\theta_1 + \varphi) \\ v_i \sin\theta_2 &= v_{o2} \sin(\theta_2 + \varphi), \end{aligned} \tag{1}$$

i.e. the back thrusts have no thickness, and cannot get thinner or thicker. Second, requiring a constant volume flux through the back thrusts yields

$$v_i e_{i1} = v_{o1} e_{o1} \qquad v_i e_{i2} = v_{o2} e_{o2}. \tag{2}$$

Velocities (v_i, v_{o1}, v_{o2}), angles (θ_1, θ_2, φ), and thicknesses (e_{i1}, e_{i2}, e_{o1}, e_{o2}) appearing in Eqs. (1) and (2) are illustrated in Fig. 2a. From Eqs. (1) and (2) above, we obtain the thickness changes in the layers as they pass from the flat to the ramp

$$\frac{e_{o1}}{e_{i1}} = \frac{\sin(\theta_1 + \varphi)}{\sin\theta_1} \qquad \frac{e_{o2}}{e_{i2}} = \frac{\sin(\theta_2 + \varphi)}{\sin\theta_2}, \tag{3}$$

which provide a simple way to determine the dips θ_1 and θ_2 merely by measuring the thicknesses before and after crossing the back thrusts. Note that in kinematic models (Suppe, 1983), $\theta_1 = \theta_2 = (\pi - \varphi)/2$, and thus $e_{o1} = e_{i1}$ and $e_{o2} = e_{i2}$ from Eq. (3).

2.2. Forces

We adopt a purely frictional (Coulomb) behavior of the materials, i.e. non-elastic, perfectly plastic. Thus only a friction angle and cohesion are required to describe the material at and beyond failure. α_{R1} is the friction angle of the material of layer 1 against ramp 1 (or lower). α_{R2} is the

friction angle of the material of layer 1 against the material of layer 2. α_{B1} and α_{B2} are the internal friction angles of the materials of layers 1 and 2, respectively. c_{R1}, c_{R2}, c_{B1}, and c_{B2} are the respective cohesions. The global force equilibria of the two parts of the hanging wall above the ramp (parts (ABDE) and (BCD); Fig. 2b), read, respectively:

$$\mathbf{P}_1 + \mathbf{F}_{R1} - \mathbf{F}_{R2} + \mathbf{F}_{B1} = 0 \qquad \mathbf{P}_2 + \mathbf{F}_{R2} + \mathbf{F}_{B2} = 0. \tag{4}$$

The solution to this set of equations is developed in detail in the Appendix.

2.3. Dissipations

With the aforementioned assumption that all deformation occurs along the thrust planes, only four sources of dissipation must be considered: D_{R1} and D_{R2} along ramps 1 and 2, and D_{B1} and D_{B2} along back thrusts 1 and 2, respectively. Each is defined as the product of the shear force acting parallel to the thrust with the jump in tangential velocity across the thrust:

$$\begin{aligned} D_{R1} &= T_{R1} v_{o1} \qquad D_{R2} = T_{R2} |v_{o2} - v_{o1}| \\ D_{B1} &= T_{B1}(v_{o1} \cos(\theta_1 + \varphi) - v_i \cos\theta_1)) \\ D_{B2} &= T_{B2}(v_{o2} \cos(\theta_2 + \varphi) - v_i \cos\theta_2)). \end{aligned} \tag{5}$$

Full expressions for the shear forces T_{R1}, T_{R2}, T_{B1}, and T_{B2} are given in the Appendix. T_{R1} is also illustrated in Fig. 2b. The total dissipation is thus:

$$D = D_{R1} + D_{R2} + D_{B1} + D_{B2} = F v_i, \tag{6}$$

where

$$F = \frac{1}{2} \rho g e_{i1} e_{i2} (k_{R1} + k_{R2} + k_{B1} + k_{B2}) \tag{7}$$

is the force conjugate to v_i in the sense of dissipation. The functions $k_{R1,R2,B1,B2}(\varphi, \theta_1, \theta_2, \alpha_{R1}, \alpha_{R2}, \alpha_{B1}, \alpha_{B2}, c_{R1}, c_{R2}, c_{B1}, c_{B2}, e_{i1}, (e_{i2})$ are not written for the sake of conciseness, but can be easily retrieved from the definitions of dissipations (5)–(7), and, in the Appendix, the Coulomb relations (12), and the solution (14)–(17).

2.4. Optimal back thrust dips

The last stage is to minimize the total dissipation (6) with respect to the thrust dips θ_1 and θ_2. The optimal dips are thus

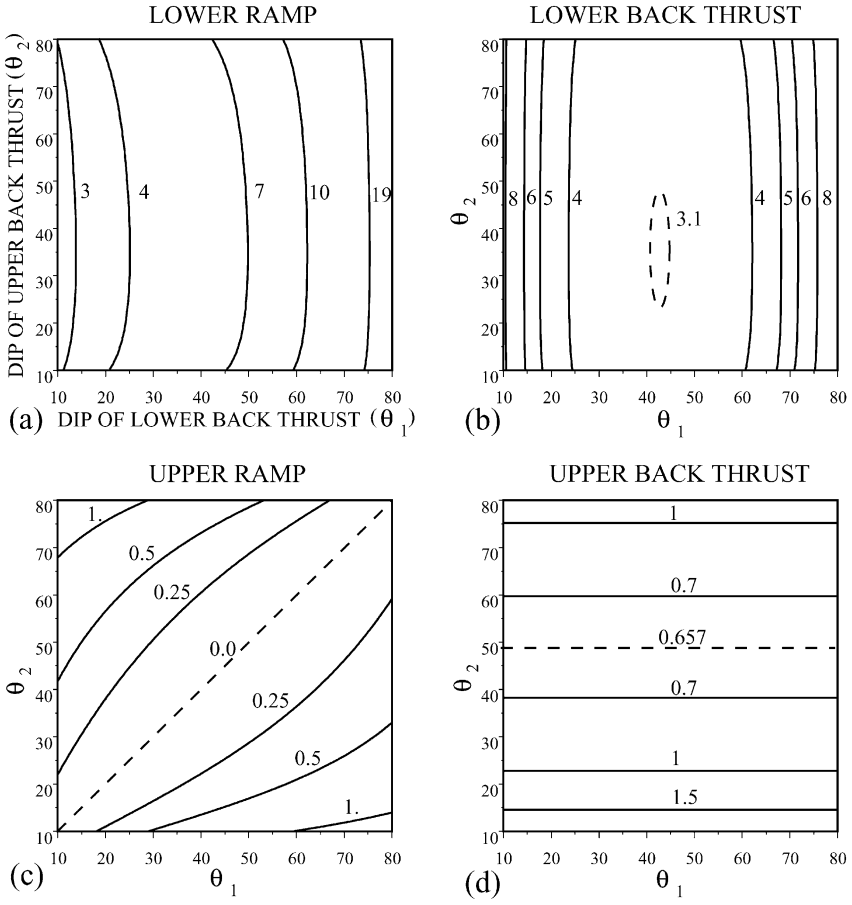

Fig. 3. The four sources of dissipation as functions of the back thrust dips θ_1 and θ_2. The dashed lines indicate the minimum values, where applicable.

solutions of the coupled equations

$$\frac{\partial k}{\partial \theta_1} = 0 \text{ and } \frac{\partial k}{\partial \theta_2} = 0, \quad (8)$$

where $k = k_{R1} + k_{R2} + k_{B1} + k_{B2}$ is the total dimensionless dissipation. Unfortunately, these lengthy coupled equations do not have analytic solutions and must be solved numerically using a root finding, or a minimization method. We chose here a minimization method on the function k using a mathematical free software (www.scilab.org). It should be noted that $k_{R1,R2,B1,B2}$ are only functions of the dips of the ramps and back thrusts, of the eight friction parameters (friction angles and cohesions), and of the thickness ratio e_{i1}/e_{i2}. The optimal dips are thus independent of the volumic mass of the materials, and of the absolute values of thicknesses. Furthermore, the analysis of Maillot and Leroy (2003) showed that they are also independent of the flat thrust length (line HE in Fig. 2a).

2.5. Example of dissipation analysis

As an example, we take a set of parameters that is very close to our experiments: the ramp dips at 30°, layer 1 (lower layer) has an internal friction angle $\alpha_{B1} = 30°$, a friction on the ramp 1 $\alpha_{R1} = 33°$, a friction with layer 2 (upper) $\alpha_{R2} = 22°$, and the layer 2 (upper) has an internal friction angle $\alpha_{B2} = 30°$. All cohesions are set to zero. The thicknesses of layers 1 and 2 are $e_{i1} = 10$ mm and $e_{i2} = 9.5$ mm, respectively. From these parameters, we can compute the four sources of dissipation as functions of θ_1 and θ_2 and examine their respective effects on the optimal dips. The four normalized dissipations (i.e. the functions k_{R1}, k_{R2}, k_{B1}, and k_{B2}) are each illustrated in Fig. 3, while Fig. 4 shows their sum, of which the minimum gives the optimal dips (indicated by the dashed lines). Several comments are now in order. First, dissipation along the lower ramp (Fig. 3a) is relatively insensitive to the upper back thrust dip, and strongly dependent on the lower back thrust dip, for which it promotes very low dips ($\theta_1 < 10°$). Second, dissipation along the lower back thrust (Fig. 3b) is even more insensitive to the upper back thrust dip, and tends to promote intermediate values of the lower back thrust dip (around 42°). Third, dissipation along the upper ramp (Fig. 3c) is equally sensitive to θ_1 and θ_2, and promotes a geometry where $\theta_1 = \theta_2$, regardless of their actual values. In other words, it promotes the development of a single planar back thrust through the two layers. If this happens, then we can see from Eq. (1) that $v_{o1} = v_{o2}$, and that therefore, from Eq. (5), second equality, the dissipation D_{R2} along the upper ramp is exactly null. Of the four sources of dissipation, it is the only one that can disappear because the upper ramp can be locked, but none of the others. Fourth, dissipation along the upper back thrust (Fig. 3d) is completely insensitive to θ_1, and promotes intermediate values of θ_2 (around 50°), similarly to the dissipation along the lower back thrust with respect to θ_1. Finally, dissipations in the lower layer (Fig. 3a and b) are approximately 10 times higher than those in the upper layer (Fig. 3c and d), and we, therefore, expect θ_1 to be better constrained than θ_2.

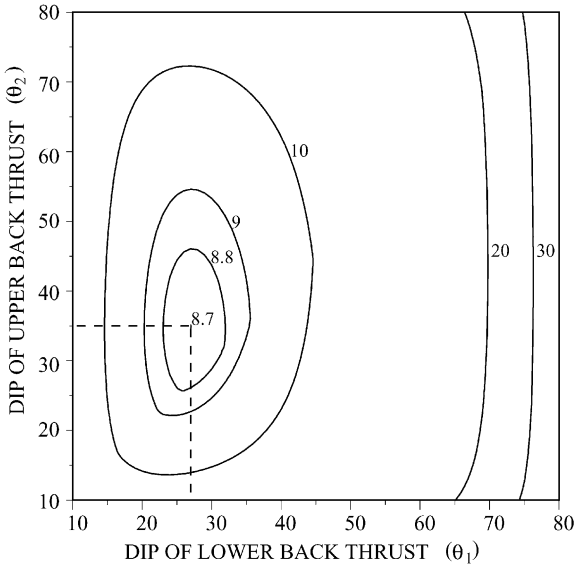

Fig. 4. Total dissipation as a function of the back thrust dips θ_1 and θ_2. $\theta_1 \approx 27°$, and $\theta \approx 35°$ are the optimal dips in the sense of dissipation.

Fig. 4 shows the sum of all sources of dissipations. The total dissipation now shows clearly a minimum ($k_{min} = 8.7$) that defines uniquely the optimal dips $\theta_1 = 27°$ and $\theta_2 = 35°$. The contour curve 8.8 is only 1.15% higher than the minimum, and indicates the range of dips θ_1 and θ_2 that would produce a total dissipation that is within 1.15% of the minimum. This range is large: $23° \leq \theta_1 \leq 32°$, and, as expected, larger for θ_2: $26° \leq \theta_2 \leq 45°$. This apparently suggests that minimizing the dissipation does not yield strong constraints on the thrust dips. In fact, the experimental results (Section 4), will prove to be, on average, all within 3° of the theoretically optimal dips.

Since our experiments were designed to highlight the effect of the friction on the lower ramp, we first show this effect in the theoretical example, with the help of Fig. 5. Keeping the parameters of the example unchanged, and letting only the friction angle of the lower ramp, α_{R1}, vary from 0 to 50°, yields optimal back thrust dips that decrease from 60 to 20°. For $\alpha_{R1} \leq \alpha_{R2} = 22°$, $\theta_1 = \theta_2$, a single back thrust develops, and the upper ramp is not activated (Fig. 3c). When $\alpha_{R1} > \alpha_{R2} = 22°$, then $\theta_1 < \theta_2$, the lower back thrust is refracted into a steeper back thrust in the upper layer, and the upper ramp is activated. In this situation of thrust refraction, the upper back thrust becomes independent of the lower ramp, its dip being essentially controlled by the friction on the upper ramp. Since our analogue materials exhibit small amounts of cohesion, we also show on this plot the effect of adding a cohesion of 50 Pa on the lower ramp: the optimal thrust dips are decreased by 3° to 20°, and the thrust refraction occurs for a lower value of α_{R1}, but the qualitative behavior remains the same. For comparison, we

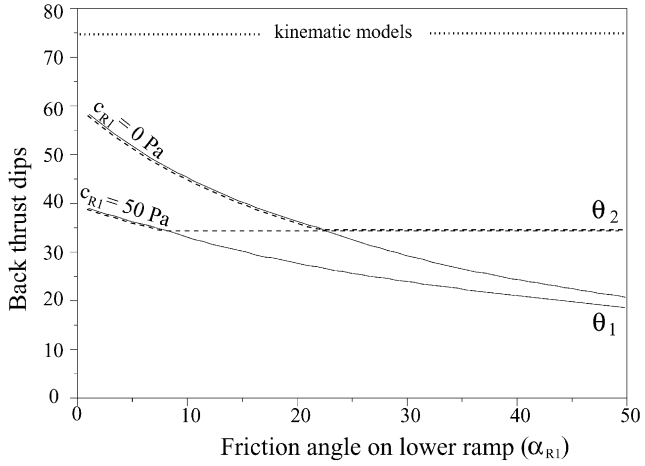

Fig. 5. Illustration of the effect of the friction on the lower ramp (α_{R1}) on the back thrust dips θ_1 (solid lines) and θ_2 (dashed lines), assuming a cohesion c_{R1} of 0 and 50 Pa. For comparison, the dotted line indicates the back thrust dips assumed in kinematic models.

indicate as a dotted line the back thrust dips that would be assumed in classical kinematic models of fault-bend folds that disregard the effect of friction.

3. Description of experiments

A series of six experiments was made to test the validity of the theory presented above. A generic initial and final state of experiment is illustrated in Fig. 1. A model made of two layers of Nemours sand separated by a thin layer of micro glass beads, with respective thicknesses of 10, 1, and 9 mm is placed in a 200×200×100 mm plexiglass box in which a rigid plexiglass ramp was installed beforehand (line (EA) in Fig. 2). The glass beads layer plays the role of a second ramp (line (GDB) in Fig. 2). In all experiments we have tried to be consistent during the preparation of the layers; pouring sand in small amounts on the surface of the model and scraping the sand pile to a horizontal layer, not more than 3 mm thick at a time. Colored marker horizons (each about 0.1–0.3 mm thick) were sprinkled on the surface after each scraping step, to act as strain markers. This somewhat laborious procedure has the central advantage of providing reasonably reproducible samples.

The list of actual models prepared with this procedure is given in Table 1. In experiments 2–4, we fix the rigid ramp dip at $\varphi = 30°$, and vary the friction along it. In experiment 2, a P150 sandpaper was glued on the ramp, providing a higher friction than the internal sand friction. In experiment 3, a fiberglass sheet was glued on the ramp, providing an intermediate friction. In experiment 4, the ramp was slid under a fiberglass sheet above which the model was placed, thus providing a zero friction surface since there was no relative displacement between the sand and the fiberglass sheet during the transport of the sand layers over the ramp. The measurement of these friction parameters is detailed in Section 4. Experiments 8, 7, and 9, are, respectively, identical to experiments 2, 3, and 4, but with a rigid ramp dipping at $\varphi = 45°$.

Every model was then shortened by pushing the rigid ramp into the model at a constant velocity $v_i = 22$ cm/h. The shortening was stopped every 10 mm to remove any material forming a relief, with the same scrapping apparatus as that used to prepare the model (the maximum relief height was around 5 mm). The total applied shortening was in all cases sufficient to reach a steady state in the model. Once the maximum shortening allowed by the geometry of the box was reached, the final relief build up was not scrapped, the model was wetted, then cut parallel to the shortening direction (i.e. perpendicular to the ramp), then photographed to analyze in detail the geometry of the back thrusts and compare it with the theoretical predictions. This is discussed in Section 4.

3.1. Properties of experimental materials

In order to test our dissipation theory against the experiments, we measured the failure envelopes of the experimental materials. This was done independently of the experiments, but also in conditions as close as possible to

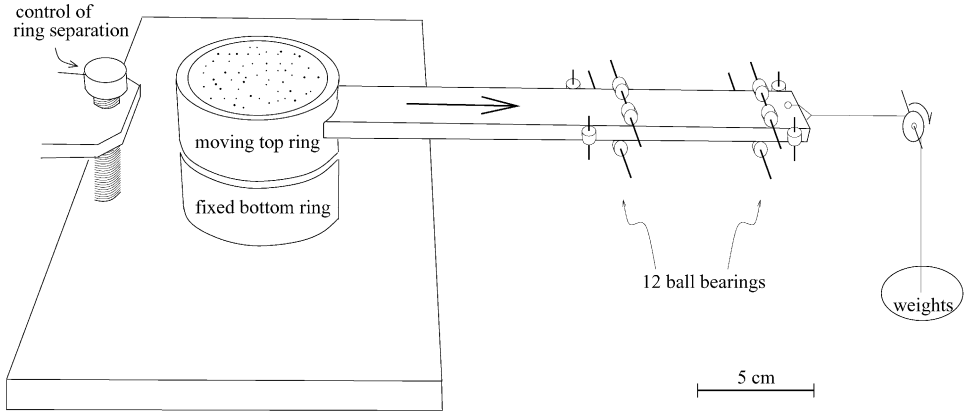

Fig. 6. Schematic diagram of the apparatus designed to measure friction coefficients at low stresses.

the experimental ones, i.e. at stresses below 1 kPa. This is why the failure envelopes (friction coefficient and cohesion) were determined with a specifically designed apparatus illustrated in Fig. 6. The two plexiglass rings, separated just enough not to touch each other, are filled by slowly pouring in the granular material. The top ring (of internal diameter 68 mm and height 35 mm) is then pulled horizontally, i.e. parallel to the fixed bottom ring, by adding weights at the other end of the string on which it is attached (right side of Fig. 6). The plexiglass bar between the ring and the string is held by 12 ball bearings ensuring a precise translation of the ring without rotation, and with very little friction (about 10 g where needed to move the top ring in the absence of granular material). We interpret as the peak shear load the lowest weight sufficient to trigger a large irreversible movement of the top ring. These weights were determined to within about 10 g. We then start again the whole procedure several times, adding increasing weights on a lid placed on the top surface of the granular material. The weights are then converted to normal and shear stresses. This measurement procedure is essentially the same as that proposed by Schellart (2000).

The Nemours sand used in the models was provided by the Division Géologie, Géochimie of the Institut Français du Pétrole. It is a natural sand sieved between 80 and 120 μm with a sharp peak at 100 μm. Its density is 1.53 ± 0.02. The grain size of the micro glass beads, the second granular material used in the models, ranges between 50 and 100 μm, and its density is 1.46. Densities were measured by slowly pouring the material into a container similar to our friction apparatus. The internal frictions of the Nemours sand and the glass beads are computed from a linear regression of the data with error bars shown in Fig. 7. In terms of friction angles, this gives 30.3–32.8° for the Nemours sand, and 18.7–22.8° for the glass beads. The cohesions are, respectively, 80 ± 22, and 79 ± 29 Pa. They prove to be relatively high compared with the stress levels of a few hundred Pascals expected in the experiments, and they are accounted for in the theoretical approach. The friction of the Nemours sand against the P150 sandpaper and the fiberglass sheet was determined in the same way, simply replacing the bottom ring by a plexiglass board on which we glued the material to be tested. The results and the linear regression are shown in Fig. 8. In terms of friction angles, this gives 34.5–34.8° for the sandpaper and 22.8–23.3° for the fiberglass sheet, with respective cohesions of -20 ± 6 and 51 ± 11 Pa, as listed in Table 1.

Our measurement method has drawbacks that we discuss now. First, by measuring only the peak shear load, and, therefore, ignoring the strain-softening, we probably overestimate the friction on the imposed ramp which is continuously active. This is consistent with our theoretical approach, which assumes a constant friction, and will be further discussed in Section 4. Second, the deposition procedure of the sand does not include the scrapping step used in the construction of the models, and the shear surface is horizontal, whereas it is oblique in the models. Although not measurable with our method, these differences can only have a small effect in view of the fit between experiments and theory that we present in Section 4. Finally, friction on the side walls of the ring apparatus reduces the normal stress applied on the tested shear surface, yielding an overestimated cohesion and an underestimated friction angle. This silo effect is, however, small because the diameter of the ring is twice its height (Mourgues and Cobbold, 2003). Furthermore, its opposite effect on the friction coefficient and the cohesion would produce a small change of our theoretical predictions, as illustrated by Fig. 5.

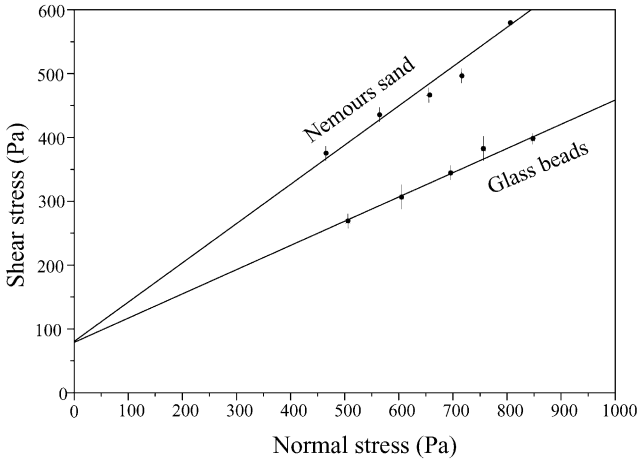

Fig. 7. Failure envelopes for the Nemours sand and the glass beads. A linear regression gives $\tau = (0.615 \pm 0.03)\sigma_n + 80 \pm 22$ (the friction angle ranges from 30.3 to 32.8°) for the Nemours sand, and $\tau = (0.38 \pm 0.04)\sigma_n + 79 \pm 29$ (the friction angle ranges from 18.7 to 22.8°) for the glass beads.

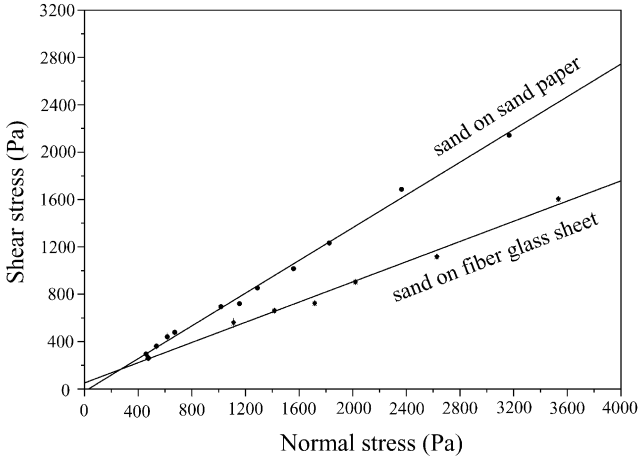

Fig. 8. Failure envelopes of the Nemours sand against P150 sand paper, and against fiber glass sheet. Linear regressions give $\tau = (0.691 \pm 0.004)\sigma_n - 20 \pm 6$ for the sand paper, and $\tau = (0.426 \pm 0.005)\sigma_n + 51 \pm 11$ for the fiber glass sheet. In terms of friction angles, the sand paper gives 34.5–34.8°, and the fiber glass sheet, 22.8–23.3°.

4. Analysis of the experiments

4.1. Methods of measurements

Seven to nine cross-sections parallel to the shortening direction were analyzed for each of the six experiments, taken roughly every 2 cm perpendicular to the strike of the ramp. The thrust dips θ_1 and θ_2 were directly measured by joining the kinks in the color markers, which are produced by the slip along the thrusts. Examples of such interpretations are shown by the oblique black solid lines in the ramp hanging walls of the experiments 2, 3, 8, and 7 (Figs. 9 and 10). For experiments 4 and 9, which were shortened above a frictionless ramp, there were no visible kinks in the layers. Therefore, we joined the points of departure from a straight line of the color markers. These are again shown as solid black lines in Figs. 9 and 10.

4.2. Fit between experiments and theory

Table 2 summarizes all mean measured and theoretical dips, and their differences. Fig. 11 is a graphical representation of all measured dips, and of the theoretical dip ranges. For each experiment (horizontal axis in Fig. 11), the first column concerns the lower back thrust dip (θ_1), and the second, the upper one (θ_2). The double-headed solid

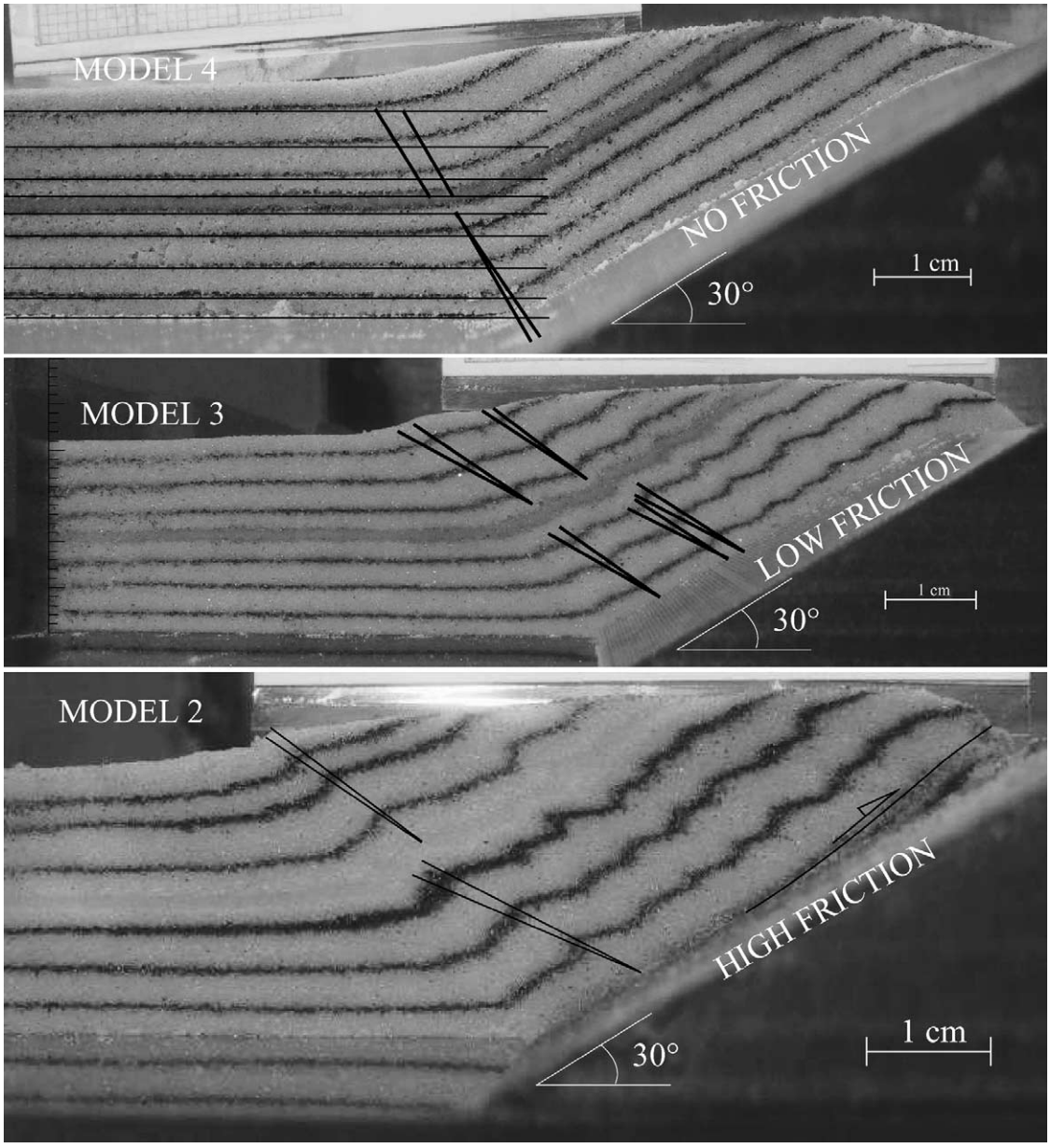

Fig. 9. Photographs of typical model cross-sections used to determine the back thrust dips in experiments 4 (top), 3 (middle), and 2 (bottom). The solid black lines represent the interpreted back thrusts. For model 4 (top), there are no kinks in the color markers, and the thrust dips were determined by joining the points of departure from a straight horizontal line of the color markers.

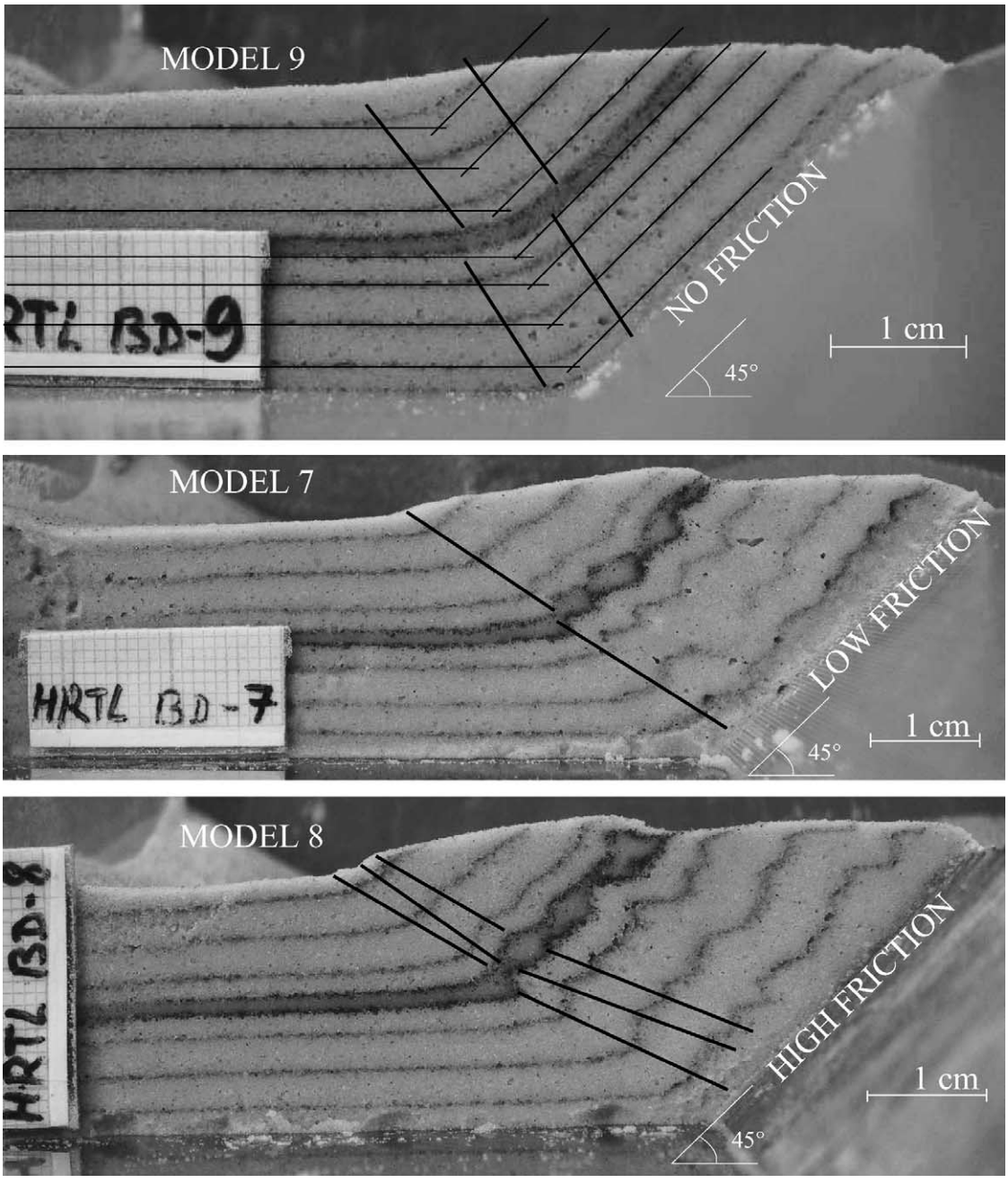

Fig. 10. Photographs of typical model cross-sections used to determine the back thrust dips in experiments 9 (top), 7 (middle), 8 (bottom). Otherwise, same caption as Fig. 9.

arrows indicate the maximum and minimum measured values. The range of these values is large (between 2 and 12°), because of the irregularity and anastomosing character of the thrusts. We will, therefore, concentrate our analysis on the mean values, indicated by the black dots. This is further justified by our theoretical approach, which considers mean forces on the thrusts and thus provides predictions of mean dips. The theoretical predictions are shown as black bars. Their sometimes large range (up to 6°) is due to the uncertainties on the material properties. This is acceptable, however, because the predicted dips of all experiments range over 30°, i.e. five times more than the larger uncertainty of a single experiment.

Fig. 11 shows that all theoretical predictions, for both lower and upper thrusts, are within the range of observed experimental dips. Furthermore, the mean observed dips for different models, ranging from 27 to 58°, are at most 3° away from the predictions (columns 6 and 7 of Table 2). We conclude that the theory predicts correctly the mean dips of the thrusts. This is in contrast to the apparently poor selectivity observed in the example of Section 2, where a variation of 5° of θ_1, or 10° of θ_2, around their optimal value

Table 2
List of experimental results, theoretical predictions, and differences between them

Exp. no.	Mean observed dips (°)		Theoretical dips (°)		Difference (°)	
	$\bar{\theta}_1$	$\bar{\theta}_2$	θ_1	θ_2	$\theta_1-\bar{\theta}_1$	$\theta_2-\bar{\theta}_2$
2	28.6	32.1	31.6–35.8	32.4–38	3	0.3
3	32.6	33.3	30.8–36.6	31.8–38	0	0
4	58.6	59	58.6–59.6	58.6–59.6	0	0
8	26.5	33.5	27.4–31.4	28.8–35.2	0.9	0
7	28.5	32.5	29.2–33.8	30–35.2	0.7	0
9	52.5	52.5	51–52.4	51–52.4	0.1	0.1

A graphical representation is given in Fig. 11.

resulted in a total dissipation only 1.15% higher than the optimal value. Here, considering the least successful experiment, BD2, the discrepancy for θ_1 is 3°, and 0.3° for θ_2. Thus, we observe that the analogue models are able to find the optimum geometry with a very high precision on the dissipated energy.

We have also deduced the back thrust dips by measuring the thickness changes of layers between the flat and the ramp and using the thickening relations (3). The dips thus obtained are consistent with, but systematically higher than those measured directly, and on average, 5° higher than the theoretical predictions. This means that there is less thickening than expected by Eq. (3), and strongly suggests that the assumption of volume conservation (2) is not adequate for the development of thrusts in dry sand, a fact acknowledged by others indeed (e.g. Lohrmann et al. (2003), for such measurements at stresses below 1 kPa). A generalization of the theory to variable densities could be envisaged, but it is not within the scope of the present article.

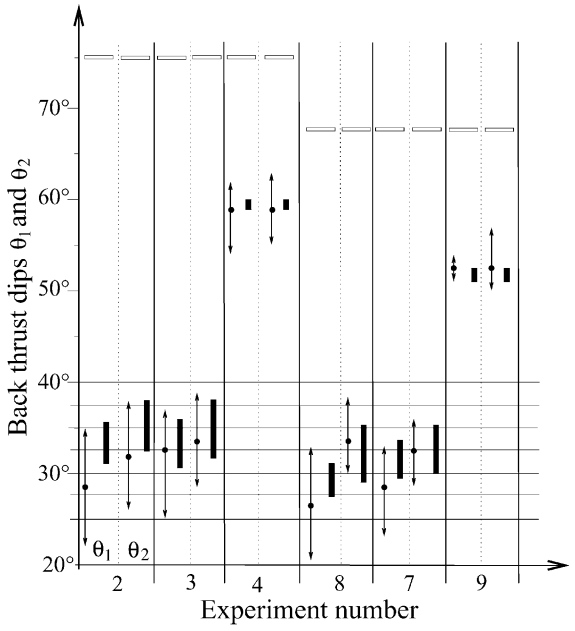

Fig. 11. Comparison between the theoretical and experimental results for all six experiments. For each experiment, the left column concerns θ_1, i.e. the lower back thrust dip, and the right column concerns θ_2, the upper back thrust dip. Solid double arrows show the minimum, maximum, and average (black dot) measured dips. The black bars show the optimal dip ranges with respect to dissipation (i.e. our theoretical predictions). The horizontal white bars show the dips assumed in most kinematic models of fault-bend folds: $\theta_1=\theta_2=(\pi-\varphi)/2$, where the ramp dip φ is 30° for experiments 2, 3, and 4, and 45° for experiments 8, 7, and 9. Hence, in kinematic models, no variation of back thrust dip is anticipated between cases with different ramp frictions.

4.3. Theoretical interpretations of the observations

Having established the validity of the dissipation theory to predict the dips observed in our experiments, we now propose some interpretations of the results in the light of the theory. We consider the effects of the ramp friction, and dip.

The comparison of experiments 2, 3, and 4 shows that the theoretical thrust dips (both lower θ_1 and upper θ_2) are decreasing functions of the lower ramp friction, which has a major influence on them (see also Fig. 5). The comparison of pairs of experiments, 2 and 8, 3 and 7, and 4 and 9, which have the same ramp friction but different ramp dip, shows that both thrust dips are also decreasing but smoother functions of the lower ramp dip. These theoretical tendencies are well reproduced by the mean experimental values. They can be understood as follows: as friction increases along the rigid lower ramp, or as the ramp becomes steeper, the excess dissipation in the model is reduced by reduction of the normal stress on the ramp. This is done by reducing the back thrust dip, thus enabling a better forward movement of the hanging wall, which relieves the normal stress it exerts on the ramp.

One conclusion that can be drawn from the present work is the condition under which the lower and upper back thrusts can have different dips, although they occur in the same material. In experiments 2 and 3, where friction along the ramp is high, only θ_1 is sensitive to the change in ramp friction, while in experiment 4 where ramp friction is zero, both angles are. The same can be said of experiments 8, 7, and 9, respectively (Fig. 11). The theoretical ranges of Fig. 11 describe this behavior. They show that as long as the friction on the lower ramp is less than that of the upper ramp (experiments 4 and 9), both thrusts have the same dip, and there is no slip on the upper ramp. When the lower ramp

friction increases above that of the upper ramp (experiments 2, 3, 8, and 7), then the upper ramp becomes active and imposes a steepening of the upper back thrust through the very mechanism explained above for the lower ramp. This thrust refraction resulting from the activation of a secondary upper ramp finds a clear expression in the topography of the models of experiments 7 and 8 (Fig. 10), where the two ramps produce a relief simultaneously. The effect is less pronounced for experiments 2 and 3 (Fig. 9) because the ramp is less steep, but it can still be observed on other cross-sections along strike, which are not shown here. Thus the conclusion can be summarized as

$$\begin{aligned} &\alpha_{R1} \leq \alpha_{R2} \Rightarrow \theta_2 = \theta_1 \quad \text{(planar thrust)} \\ &\alpha_{R1} > \alpha_{R2} \Rightarrow \theta_2 > \theta_1 \quad \text{(refracted thrust),} \end{aligned} \tag{9}$$

if we neglect the effect of cohesion (Fig. 5). In our experiments the cohesion is not negligible compared with the magnitudes of the acting forces, but it is negligible in real structures. The generalization of the present theory to any number of layers, and the parametric study for three layers (Luu, 2003; Luu et al., 2004) have reached these conclusions, which, again, can now be considered to be validated by the present experiments. The fact that $\theta_2 < \theta_1$ does not happen throughout the six experiments, and cannot happen theoretically, has an interesting consequence: the back thrusts will always be refracted so as to define an overall shape that is concave upwards. Because of the velocity compatibility (1), the upper hanging wall will always rise as fast as, or faster than, the lower one. This remains theoretically true for ramp hanging walls made of any number of layers, where the activation of secondary upper ramps is more widely referred to as bedding-parallel slip. This constitutes a possible explanation of the top-to-foreland sense of shear observed in the hanging wall of ramp related folds.

The empty rectangles in Fig. 11 indicate the back thrust dips generally assumed in kinematic models of fault-bend folds. They bisect the lower flat-ramp angle ($\theta_1 = \theta_2 = (\pi - \varphi)/2$), so as to conserve the thickness between the flat and the ramp. Obviously, these assumptions are not valid in our experimental fault-bend folds. First because there is thickening, both observed and predicted by our theory (although the latter is overestimated), and second, because the dips depend less on the ramp dip than on the ramp friction, which cannot be taken into account in kinematic models. These remarks have potentially important consequences on the balancing of cross-section using these

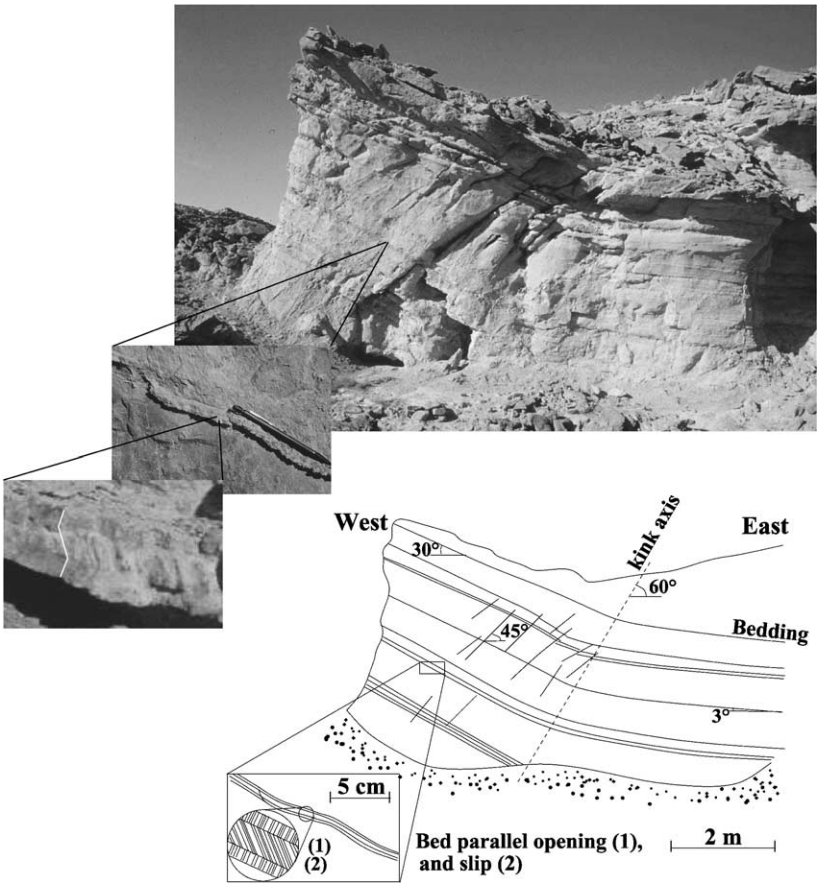

Fig. 12. An example of kink fold in the Gushi Marls (Miocene) of the Iranian Makran. After crossing the kink axis towards the west, the marls exhibit thickening and top-to-foreland (westward) bed parallel slip (inset), materialized by inter-bed calcite growth. Photographs and measurements by Prof. Siegfried Lallemant of the University of Cergy-Pontoise.

models, or on the determination of blind thrust geometries from the surface topography as proposed by Savage and Cooke (2003).

Persson (2001) made various observations on the spatial periodicity of the thrusts developing above a rigid ramp, but with a single type of ramp surface (plexiglass). Hence, in the current models, the important effect of the ramp friction on the periodicity of the thrusts is highlighted: in experiments 4 and 9 (frictionless ramp), the thrusts form continuously because there are no visible kinks in the color markers, in contrast to the four other experiments. However, this important question of back thrust periodicity in the ramp hanging wall cannot be addressed with the present form of our theory, because it is probably related to the strain-softening characteristics of our materials, which are not accounted for in the present study.

Finally, we present a field example that illustrates qualitatively some of our conclusions. Fig. 12 shows a synclinal kink in the Gushi Marls (Miocene) of the Iranian Makran, by the village of Gaz (GPS: 26°05′57″ N, 57°16′12″ E). The fold axis is horizontal with an azimuth N 155°, and the marls slide from East to West, first on the lower flat dipping 3° to the East, then on the ramp dipping 30°, thus forming a kink fold, with an axial plane dipping 60° to the West. After passing the kink axis, the marl layers exhibit numerous tension gashes parallel to the bedding, which are filled with calcite fibers. The fibers indicate first an opening perpendicular to the bedding (equivalent to an overall thickening of the beds), then top-to-foreland slip added to the opening (oblique fibers). This thickening is consistent with the dip of the kink axis (60°), which is substantially less than the bissector of the fold (73°, as would be assumed in kinematic models), and implies therefore thickening of the beds. Both observations (thickening and slip) are consistent with the behavior of our analogue models, and with our theory. Of course, the deformation of the Gushi Marls is essentially ductile (despite the occurrence of a few fractures dipping at 45°), in contrast with our frictional models. The more appropriate ductile version of the theory leads to the same conclusions about thickening and bed-parallel slip (Maillot and Leroy, 2003).

5. Conclusion

The six analogue experiments presented here were designed to study the passage of a two layer frictional material from a horizontal lower flat to a ramp, and to validate the mean dissipation theory of Maillot and Leroy (2003). The mean thrust dips forming in each layer of the models spread over 30°, and are reproduced by the dissipation theory to within 3°, thus validating it. These dedicated experiments were necessary to validate the theory because published analogue experiments often address much more complex structures, do not provide all relevant friction data, or provide them in stress conditions that are too far from the experimental ones (Schellart, 2000). These experiments also allow us to draw conclusions with a geological relevance. We showed that both observed and predicted thrust dips are much lower than those assumed in kinematic models. Such differences are significant when balancing cross-sections or interpreting surface topography using these models. Our models and theoretical results show that the ramp friction has a 'first order' effect on the size, thickness, and velocity of its hanging wall. Maximum thickening, and minimum velocity, are observed in the experiment with highest ramp friction and steepest ramp.

Both lower and upper thrust dips appear to be decreasing functions of the dip and friction on the ramp, the latter showing a very pronounced effect. Furthermore, slip between the two layers can only occur if friction is lower than that on the ramp. This is also the condition for thrust refraction across the beds, and constitutes a possible mechanism for the 'top-to-foreland' sense of shear observed in the hanging wall of fault-bend folds.

The good fit of the optimal thrust dips to the observed ones is a remarkable result when considering the simplicity of the theory that is presented here in a self-consistent manner. In the theoretical approach, we did not take into account geometrical changes, strain-softening, and dilation/compaction due to slip on the thrusts. No finite-element discretization is required, and the main kinematic features are adopted from the kinematic models, and then optimized through an essentially analytic approach. The dissipation theory first proposed by Merchant (1944, 1945), adapted by Maillot and Leroy (2003) to frictional and to ductile materials, and validated here for frictional materials, offers therefore a method to improve the kinematic models and to interpret the analogue models by introducing the concepts of global force balance and of minimum dissipation, through simple and versatile procedures.

Acknowledgements

This work was initiated during Hemin Koyi's sabbatical stay as an invited professor by the scientific council of the University of Cergy-Pontoise (UCP). The visit of B. Maillot to Uppsala was further supported by the research contract No. 28 584 between the Institut Français du Pétrole and the UCP. Special thanks to Jean-Marc Daniel and Jean-Marie Mengus (Div. Géologie-Géochimie, Institut Français du Pétrole) for enlightening discussions and for providing us with the frictional materials. We are grateful to Prof. Siegfried Lallemant who, while in the field for other concerns, has identified a relevant outcrop from the sole description of our theoretical model.

Appendix. Resolution of the global force balance

We solve here the two global force balance equations (4), also illustrated in Fig. 2. First, the weights of the lower and upper hanging walls can be deduced directly from Fig. 2a:

$$P_1 = \rho g e_{i1}\left(\frac{1}{2}e_{i1} + e_{i2}\right)\frac{\sin(\theta_1+\varphi)}{\sin\theta_1 \sin\varphi}$$
$$P_2 = \rho g \frac{1}{2} e_{i2}^2 \frac{\sin(\theta_2+\varphi)}{\sin\theta_2 \sin\varphi}. \quad (10)$$

Second, the forces acting along the four thrusts can be expressed as a normal (N) and a tangential (T) component with respect to each thrust. This decomposition is illustrated in Fig. 2b for $\boldsymbol{F}_{R1}$. Developing all force components in the (x, y) framework (Fig. 2a) in terms of their normal and tangential components yields:

$$\begin{aligned}
F_{R1_x} &= -\cos\varphi T_{R1} - \sin\varphi N_{R1}\\
F_{R1_y} &= -\sin\varphi T_{R1} + \cos\varphi N_{R1}\\
F_{R2_x} &= -\cos\varphi T_{R2} - \sin\varphi N_{R2}\\
F_{R2_y} &= -\sin\varphi T_{R2} + \cos\varphi N_{R2}\\
F_{B1_x} &= +\cos\theta_1 T_{B1} + \sin\theta_1 N_{B1}\\
F_{B1_y} &= -\sin\theta_1 T_{B1} + \cos\theta_1 N_{B1}\\
F_{B2_x} &= +\cos\theta_2 T_{B2} + \sin\theta_2 N_{B2}\\
F_{B2_y} &= -\sin\theta_2 T_{B2} + \cos\theta_2 N_{B2}.
\end{aligned} \quad (11)$$

Note that F_{R1_x} corresponds to the horizontal shortening force applied to the moving rigid ramp by the electric motor of the sand box (if we neglect the friction of the rigid ramp on the floor and side walls of the box). The force components tangential to the thrusts are related to the normal components through the Coulomb relation $\tau = \tan\alpha\sigma_n + c$, after integration over the thrust lengths:

$$\begin{aligned}
T_{R1} &= \tan\alpha_{R1} N_{R1} + c'_{R1} \qquad T_{R2} = \tan\alpha_{R2} N_{R2} + c'_{R2}\\
T_{B1} &= \tan\alpha_{B1} N_{B1} + c'_{B1} \qquad T_{B2} = \tan\alpha_{B2} N_{B2} + c'_{B2},
\end{aligned} \quad (12)$$

where

$$\begin{aligned}
c'_{R1} &= c_{R1}\frac{e_{i1}+e_{i2}}{\sin\varphi} \qquad c'_{R2} = c_{R2}\frac{e_{i2}}{\sin\varphi}\\
c'_{B1} &= c_{B1}\frac{e_{i1}}{\sin\theta_1} \qquad c'_{B2} = c_{B2}\frac{e_{i2}}{\sin\theta_2},
\end{aligned} \quad (13)$$

are the cohesions of the thrusts multiplied by their respective lengths. Note that the quantities in (12) are total shear forces acting on the thrusts, not stresses. Then, combining Eqs. (11)–(13) with equilibrium equations (4) yields four equations with the four unknowns N_{R1}, N_{R2}, N_{B1} N_{B2}. The solutions are

$$\begin{aligned}
N_{R1} = {} & \frac{\cos\alpha_{R1}}{\sin(\theta_1+\varphi+\alpha_{B1}+\alpha_{R1})}\left[\frac{\sin(\theta_1+\varphi+\alpha_{B1}+\alpha_{R2})}{\sin(\theta_2+\varphi+\alpha_{B2}+\alpha_{R2})}\right.\\
& \times(P_2\sin(\theta_2+\alpha_{B2}) + c'_{B2}\cos\alpha_{B2}\\
& - c'_{R2}\cos(\theta_2+\varphi+\alpha_{B2})) + P_1\sin(\theta_1+\alpha_{B1})\\
& \left. - (c'_{R1} - c'_{R2})\cos(\theta_1+\varphi+\alpha_{B1}) + c'_{B1}\cos\alpha_{B1}\right]
\end{aligned} \quad (14)$$

$$\begin{aligned}
N_{B1} = {} & \frac{\cos\alpha_{B1}}{\sin(\theta_1+\varphi+\alpha_{B1}+\alpha_{R2})}\left[\frac{\sin(\alpha_{R1}-\alpha_{R2})}{\sin(\theta_2+\varphi+\alpha_{B2}+\alpha_{R2})}\right.\\
& \times(P_2\sin(\theta_2+\alpha_{B2}) + c'_{B2}\cos\alpha_{B2}\\
& - c'_{R2}\cos(\theta_2+\varphi+\alpha_{B2})) + P_1\sin(\varphi+\alpha_{R1})\\
& \left. + (c'_{R1} - c'_{R2})\cos\alpha_{R1} - c'_{B1}\cos(\theta_1+\varphi+\alpha_{R1})\right],
\end{aligned} \quad (15)$$

$$\begin{aligned}
N_{R2} = {} & \frac{\cos\alpha_{R2}}{\sin(\theta_2+\varphi+\alpha_{B2}+\alpha_{R2})}[P_2\sin(\theta_2+\alpha_{B2})\\
& + c'_{B2}\cos\alpha_{B2} - c'_{R2}\cos(\theta_2+\varphi+\alpha_{B2})],
\end{aligned} \quad (16)$$

$$\begin{aligned}
N_{B2} = {} & \frac{\cos\alpha_{B2}}{\sin(\theta_2+\varphi+\alpha_{B2}+\alpha_{R2})}[P_2\sin(\varphi+\alpha_{R2})\\
& - c'_{B2}\cos(\theta_2+\varphi+\alpha_{R2}) + c'_{R2}\cos\alpha_{R2}].
\end{aligned} \quad (17)$$

Eqs. (14)–(17), along with the Coulomb relations (12), give the solution of the global force balance (4) in terms of the mean forces along the thrusts.

References

Bonini, M., Sokoutis, D., Mulugeta, G., Katrivanos, E., 2000. Modelling hanging wall accommodation above rigid thrust ramps. Journal of Structural Geology 22, 1165–1179.

Boyer, S.E., 1986. Styles of folding within thrust sheets: examples from the Appalachian and Rocky mountains of the USA and Canada. Journal of Structural Geology 8 (3/4), 325–339.

Buil, D., 2002. L'approche cinématique du plissement naturel: intérêts et limites. Développements autour de la notion de 'Trisher'. PhD thesis, University of Cergy-Pontoise.

Cristallini, E.O., Allmendinger, R.W., 2002. Backlimb trishear: a kinematic model for curved folds developed over angular fault bends. Journal of Structural Geology 24, 289–295.

Endignoux, L., Mugnier, J.-L., 1990. The use of a forward kinematic model in the construction of balanced cross sections. Tectonics 9 (5), 1249–1262.

Erickson, J.P., Strayer, L.M., Suppe, J., 2001. Initiation and reactivation of faults during movement over a thrust-fault ramp: numerical mechanical models. Journal of Structural Geology 23, 11–23.

Laubscher, H.P., 1976. Geometrical adjustments during rotation of a Jura fold limb. Tectonophysics 36, 347–365.

Little, T.A., Holcombe, R.J., Ilg, B.R., 2002. Kinematics of oblique collision and ramping inferred from microstructures and strain in middle crustal rocks, central Southern Alps, New Zealand. Journal of Structural Geology 24, 219–239.

Lohrmann, J., Kukowski, N., Adam, J., Oncken, O., 2003. The impact of analogue material properties on the geometry, kinematics, and dynamics of convergent sand wedges. Journal of Structural Geology 25, 1691–1711.

Luu, T.T., 2003. Application du calcul à la rupture à un pli de rampe. Master's Thesis (Directors: B. Maillot and Y. Leroy), École Nationale. des Ponts et Chaussées, France.

Luu, T.T., Maillot, B., Leroy, Y.M., 2004. A mechanical analysis of the lower-flat ramp transition in a multi-layer hanging wall. XXVIth Nordic Geological Winter Meeting, Uppsala, Sweden.

Maillot, B., Leroy, Y.M., 2003. Optimal dip based on dissipation of backthrusts and hinges in fold-and-thrust belts. Journal of Geophysical Research 108 (B6), 2320–2339.

Merchant, E., 1944. Basic mechanics of the metal-cutting process. Journal of Applied Mechanics 12, 168–175.

Merchant, E., 1945. Mechanics of the Metal Cutting process. II. Plasticity conditions in orthogonal cutting. Journal of Applied Physics 16, 318–324.

Merle, O., Abidi, N., 1995. Approche expérimentale du fonctionnement des rampes émergentes. Bulletin de la Société Géologique de France 166 (5), 439–450.

Mourgues, R., Cobbold, P.R., 2003. Some tectonic consequences of fluid overpressures and seepage forces as demonstrated by sandbox modelling. Tectonophysics 376, 75–97.

Persson, K.S., 2001. Effective indenters and the development of double-vergent orogens: insights from analogue sand models. In: Koyi, H.A., Mancktelow, N.S. (Eds.), Tectonic Modelling: A Volume in Honor of Hans Ramberg. Geological Society of America Memoir 193, pp. 191–206.

Rich, J.L., 1934. Mechanics of low-angle overthrust faulting as illustrated by cumberland thrust block, Virginia, Kentucky, and Tenessee. Bulletin of the American Association of Petroleum Geologists 18 (12), 1584–1596.

Savage, H.M., Cooke, M.L., 2003. Can flat-ramp-flat fault geometry be inferred from fold shape? A comparison of kinematic and mechanical folds. Journal of Structural Geology 25, 2023–2034.

Schellart, W.P., 2000. Shear test results for cohesion and friction coefficients for different granular materials: scaling implications for their usage in analogue modelling. Tectonophysics 324, 1–16.

Suppe, J., 1983. Geometry and kinematics of fault-bend folding. American Journal of Science 283, 684–721.

Zoetemeijer, R., Sassi, W., 1992. 2D reconstruction of thrust evolution using the fault-bend fold method. In: McClay, K. (Ed.), Thrust Tectonics. Geological Society Special Publication, Chapman, London, pp. 133–140.